Unveiling the Correlation between Nanometer-Thick Molecular Monolayer Sensitivity and Near-Field Enhancement and Localization in Coupled Plasmonic Oligomers

Matthias König,[†,‡,○] Mohsen Rahmani,[†,○] Lei Zhang,[§,○] Dang Yuan Lei,[∥,⊥,*] Tyler R. Roschuk,[†] Vincenzo Giannini,[†] Cheng-Wei Qiu,[§,#] Minghui Hong,[§] Sebastian Schlücker,[‡] and Stefan A. Maier[†]

[†]Department of Physics, Imperial College London, London SW7 2AZ, United Kingdom, [‡]Department of Chemistry, University of Duisburg-Essen, Universitätsstrasse 5, 45141 Essen, Germany, [§]Department of Electrical and Computer Engineering, National University of Singapore, 4 Engineering Drive 3, Singapore, Singapore 117583, [∥]Department of Applied Physics, The Hong Kong Polytechnic University, Hung Hom, Kowloon, Hong Kong, China, [⊥]Shenzhen Research Institute, The Hong Kong Polytechnic University, Shenzhen, Guangdong, China, and [#]SZU-NUS Collaborative Innovation Center for Optoelectronic Science & Technology, Shenzhen, Guangdong 518060, China. [○]M.K., M.R., and L.Z. contributed equally to this work.

ABSTRACT Metal nanoclusters, sometimes called metamolecules or plasmonic oligomers, exhibit interesting optical properties such as Fano resonances and optical chirality. These properties promise a variety of practical applications, particularly in ultrasensitive biochemical sensing. Here we investigate experimentally the sensitivities of plasmonic pentamers and quadrumers to the adsorption of self-assembled nanometer-thick alkanethiol monolayers. The monolayer sensitivity of such oligomers is found to be significantly higher than that of single plasmonic nanoparticles and depends on the nanocluster arrangement, constituent nanoparticle shape, and the plasmon resonance wavelength. Together with full-wave numerical simulation results and the electromagnetic perturbation theory, we unveil a direct correlation between the sensitivity and the near-field intensity enhancement and spatial localization in the plasmonic "hot" spots generated in each nanocluster. Our observation is beyond conventional considerations (such as optimizing nanoparticle geometry or narrowing resonance line width) for improving the sensing performance of metal nanoclusters-based biosensors and opens the possibilities of using plasmonic nanoclusters for single-molecule detection and identification.

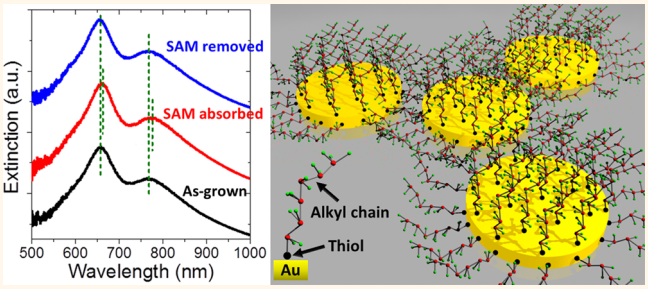

KEYWORDS: plasmonic oligomers · Fano resonance · monolayer sensing · near-field enhancement

Subwavelength nanostructures made of noble metals can sustain localized surface plasmons (LSPs) - the collective oscillations of conduction electrons at the interface between metal and dielectric materials. Upon resonant excitation of LSPs, light can be concentrated into nanoscale spatial regions around metal nanostructures, thereby largely enhancing the light-matter interaction and creating electric near-field "hot" spots. The enhanced light-matter interaction makes LSPs-based nanosensors ideal tools for spatially sensing nanoscale environment changes such as molecular-binding events,[1−3] catalytic reactions,[4] local electrochemical current,[5] phase-changing processes,[6,7] and hydrogen adsorption dynamics.[8,9] Though this is one of the unique advantages associated with LSPs in sensing applications, the sensitivity of LSPs to the refractive index of the surrounding environment is not comparable to that of commercially available sensors based on propagating surface plasmons (PSPs).[10−12] To increase the sensitivity of LSPs, great efforts have been made to optimize the size and/or shape of the metal nanoparticles.[13,14]

Electromagnetic coupling between LSPs in metal nanoparticle clusters or oligomers allows for flexible engineering of their

* Address correspondence to dylei@polyu.edu.hk.

Received for review May 27, 2014 and accepted August 19, 2014.

Published online August 19, 2014
10.1021/nn5028714

plasmonic spectral profiles, such as resonance line width and spectral contrast, and the generation of spatially controllable plasmonic "hot" spots.[15,16] Inspired by the vivid optical properties of coupled plasmonic nanoclusters, several new physical concepts and approaches, including plasmon hybridization,[17] transformation optics,[18] and subgroup decomposition,[19] have been proposed and derived to explain the optical response of such systems and to devise new nanocluster systems utilizing these coupling effects. This advancement has also significantly facilitated the design of metal nanoclusters-based sensors with sensing performance superior to individual nanoparticles.[13,15] Over the past few years, a great deal of attention has been placed in this area of spectral engineering, mainly focusing on the creation of novel plasmon resonances with much narrower spectral line widths than conventional LSPs, utilizing features and effects such as subradiant modes and Fano resonances.[20−36] Indeed, extensive theoretical and experimental investigations have collectively demonstrated that the total sensing figure of merit (FoM) of metal nanoclusters-based sensors can be mainly enhanced due to the reduced resonance line width resulting from decreased radiation damping.[22,26−29]

In addition to the advantages offered by spectral engineering, the sensitivities of nanoclusters-based sensors are also found to be much larger than those of single nanoparticles. For example, plasmonic quadrumers or pentamers, consisting of four or five identical Au nanodisks, respectively, exhibit refractive index sensitivities of up to 500−700 nm/RIU.[26,27,29,34] In comparison, the sensitivities of single Au nanoparticles, such as nanospheres, nanorods, and nanobipyramids, are generally on the order of 200−300 nm/RIU.[37−40] This sensitivity enhancement is usually believed to have resulted from the creation of multiple plasmonic "hot" spots inside the nanoclusters and the increased near-field strength. However, this explanation lacks a comprehensive understanding of how the plasmonic near-field affects the sensitivity and, more importantly, direct evidence that the near-field strength and localization determine the sensitivity. Complicating matters, bulk sensing experiments carried out in previous studies were typically performed with the nanoclusters fully immersed in liquids of different refractive indices.[26−29] The near field is highly localized around the nanocluster, and its spatial extent is in general on the order of only 10−20 nm, which indicates an interaction volume strongly limited by the field decay length. In particular, many guided self-assembly methods, such as the layer-by-layer method[41] and DNA-directed self-assembly,[42] can allow for fabrication of nanoparticle dimers and clusters with nanometer-scale interparticle distance and thus generation of stronger near-field confinement and enhancement. Thus, conventional bulk sensing approaches may not be ideally suited for studying the relationship between plasmonic near-field strength and the sensitivity due to high background relative to the enhanced signal, and hence more sophisticated methods such as monolayer sensing and molecular adsorption have to be employed for a more comprehensive understanding.[43,44]

In this work, we take a new route to study the relationship between plasmonic near-field enhancement and the refractive index sensitivity of metal nanoclusters. Self-assembled nanometer-thick alkanethiol monolayers of different carbon chain lengths were adsorbed on Au pentamers and quadrumers, and their extinction spectra were measured to extract the monolayer detection sensitivities. The sensitivity was found to depend on the nanocluster arrangement, constituent nanoparticle shape, and the plasmon resonance wavelength. Full-wave numerical simulations were performed to calculate the near-field distribution and strength in the nanoclusters at their respective resonant wavelengths, and the electromagnetic perturbation theory was used to predict the plasmon resonance shift due to the molecular monolayer adsorption. Direct comparison between the experimental and theoretical results reveals that the monolayer sensitivity for each Au nanocluster at a particular resonance wavelength is directly correlated with the spatially averaged plasmonic near-field intensity enhancement and the degree of field localization. Our observation illustrates that the overall sensing performance of metal nanoclusters-based sensors could be further boosted up by rationally engineering the plasmonic near-field confinement and amplifying the field strength, which is beyond the conventional considerations, such as changing nanoparticle geometry or reducing resonance line width for improving the sensing performance.

RESULTS AND DISCUSSION

Au nanoparticle quadrumers and pentamers were fabricated on a quartz substrate using standard electron beam lithography (EBL) process. Full experimental details are described in the Methods section. Since the plasmonic near-field distribution and enhancement in metal nanoclusters depend strongly on the size and shape of the constituent nanoparticles, four types of Au pentamers and three types of quadrumers were prepared, all comprised of a central nanodisk or square nanoparticle and outside particles of different shapes. This allows for flexible control over the near-field localization sites and the field intensity enhancement factor (EF) and hence a systematic study of the relationship between the near-field properties and the monolayer sensitivity. Figure 1 shows electron micrographs of the arrays of pentamers (a−c) and quadrumers (d−f) consisting of differently shaped nanoparticles and exhibiting repeatability and high quality of the structures over a large area. In addition, the AFM images

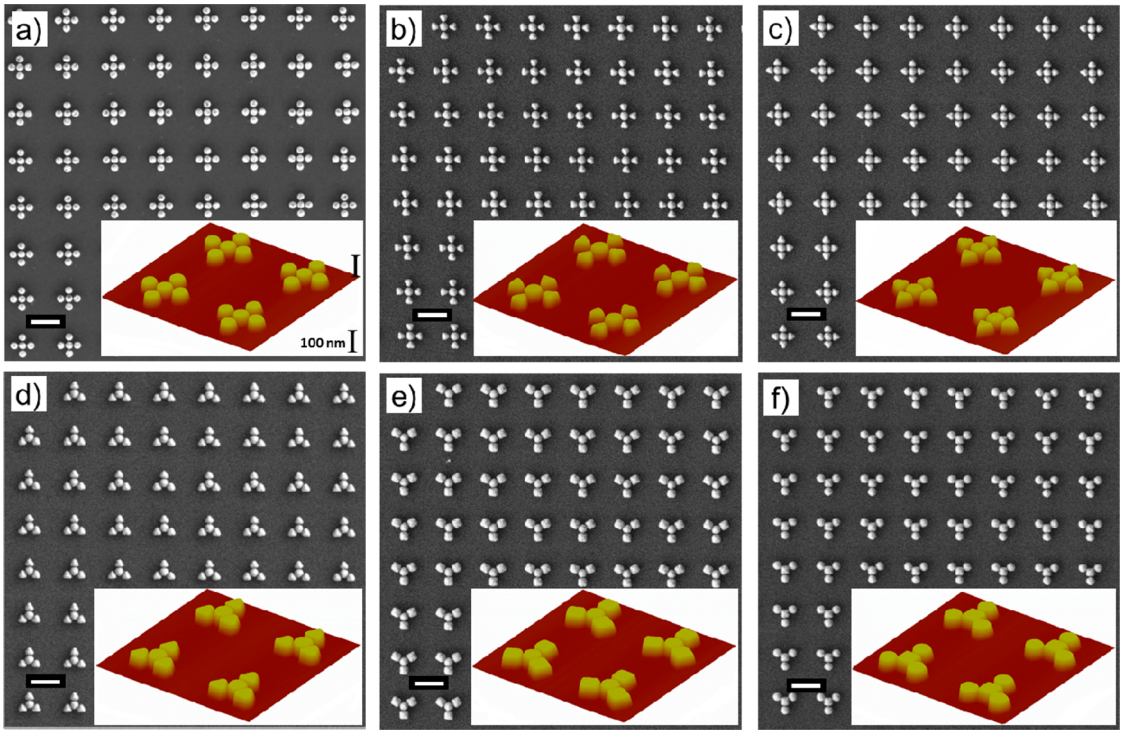

Figure 1. SEM and AFM (insets) images of gold nanoclusters under study. Three types of pentamers consist, respectively, of five identical nanodisks (a), of four inward-triangular particles and a central nanodisk (b), and of four outward-triangular particles and a central nanodisk (c). Note that the fourth type pentamer studied in the experiment is not shown here. The three types of quadrumers are comprised, respectively, of three outward-triangular particles and a central nanodisk (d), of three square particles and a central nanodisk (e), and of three nanodisks and one square particle at the center (f). The scale bars in the SEM images are 500 nm.

shown in the insets of Figure 1 reveal a good preservation of the particle shape from the top to bottom surface, enabling strong coupling between constituent nanoparticles.

To study the monolayer sensing response of the fabricated oligomers, the extinction spectra for each array of nanoclusters were collected before and after the alkanethiol monolayer adsorption by using a Fourier transform infrared (FTIR) spectroscopy system. The detailed procedures for alkanethiol monolayer adsorption and removal are described in the Methods section. Since in our experiment the same sample was used repeatedly for sensing the alkanethiol monolayers of different carbon chain lengths, it was critical to ensure that the optical response of the sample was recovered to the original after removing the adsorbed monolayer. Thus, a precalibration experiment was carried out to test the reproducibility of the sample peak position after monolayer removal, the results of which are shown in Figure 2. We can see from Figure 2a that both extinction peaks of the Au pentamer show a perceivable red-shift upon the adsorption of an alkanethiol monolayer, with the shift amount being larger for the extinction peak in the long-wavelength region than that in the short-wavelength region. After removing the self-assembled monolayer, the extinction spectrum of the Au pentamer fully overlaps with the original spectrum captured before monolayer adsorption. Figure 2b shows similar measurements conducted for the Au quadrumer sample, which shows the same behavior as that in Figure 2a. Figure 2c shows the schematics of alkanethiol molecules adsorbed on an Au quadrumer.

We then examine the monolayer sensing sensitivity for each pentamer or quadrumer nanocluster by recording their extinction spectra as a function of the carbon chain length of the adsorbed alkanethiol monolayer - varying from hexanethiol to octadecanethiol. Previous reports have pointed out that the bulk refractive index sensing sensitivity is not only dependent on the nanoparticle size and shape but also on the plasmon wavelength used in the sensing measurements, with a common feature being that a longer plasmon wavelength usually gives rise to a larger sensitivity[37,45−48] (this also holds true for propagating surface plasmon resonances[48,49]). To minimize this unwanted effect of wavelength-dependent sensitivity, we have deliberately designed the Au pentamers and quadrumers with their plasmon resonance positions varying in a very small wavelength range (between 700 and 750 nm for the long-wavelength peak of the Au pentamers, for example). Figure 3 presents the extinction spectra for the four types of Au pentamers coated with alkanethiol monolayers, each set of which shows a gradual red-shift in the two extinction peaks with increasing the carbon chain

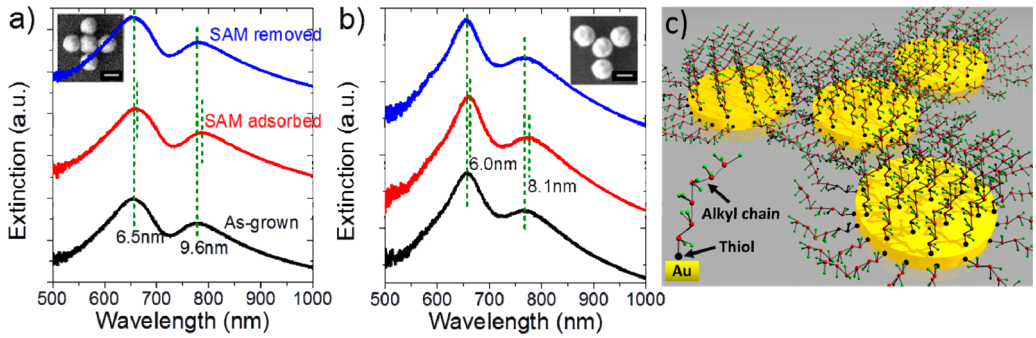

Figure 2. Precalibration of the monolayer sensing experiments using Au nanoclusters. Extinction spectra of the gold pentamer (a) and quadrumer (b) with their electron micrographs shown in the insets: black curves, as-grown nanoclusters; red curves, nanoclusters with self-assembled monolayer (SAM) adsorbed; blue curves, nanoclusters after removing SAM by the technique described in the Methods section. The dashed green lines indicate the extinction peak positions which are picked up manually at the maximum extinction intensity. The scale bar in each image is 100 nm. (c) Schematic representation of a gold quadrumer adsorbed with an alkanethiol monolayer.

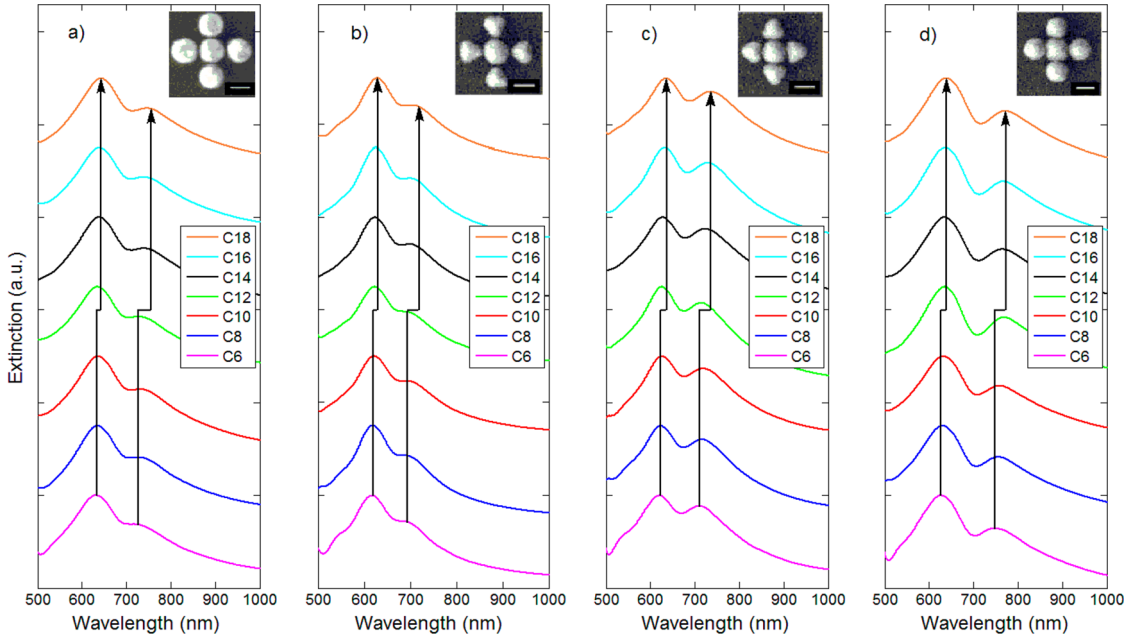

Figure 3. Plasmon resonance shift sensing the carbon chain length of different alkanethiols. Extinction spectra of the Au pentamers consisting of differently shaped nanoparticles with adsorbed SAMs of different carbon chain lengths (a–d). In each figure, from bottom to top, the adsorbed monolayers are 1-hexanethiol (C6), 1-octanethiol (C8), 1-decanethiol (C10), 1-dodecanethiol (C12), 1-tetradecanethiol (C14), 1-hexadecanethiol (C16), and 1-octadecanethiol (C18) molecules. The insets show SEM images of the Au pentamers used in each case. The scale bar in each image is 100 nm. The black arrows are guide-to-the-eyes, indicating the total resonance shift between the top and bottom spectra.

length. Previous ellipsometry studies have shown that the thickness of alkanethiol SAMs formed on polycrystalline gold changes linearly from 0.8 to 2.0 nm when increasing the number of carbons from 6 to 18.[44,50] Thus, one expects that the whole monolayer is immersed inside the plasmonic near-field region and contributes to the observed red-shift in the extinction spectra due to the change of the local environment.

To determine the monolayer sensitivity of the Au pentamers quantitatively, we plot the extinction peak shift as a function of the carbon chain length in Figure 4 and extract the sensitivity by calculating the slope of a linear fit to the measured data points. The results shown in Figure 4 illustrate that the long-wavelength extinction peak shift for each nanocluster is significantly greater than that of the short-wavelength peak, which is consistent with previous observations.[37,40,45–48] This effect can be attributed to the fact that the longer penetration of the electromagnetic field inside the dielectric at longer resonant wavelengths provides a larger interrogation volume that is sensitive to the refractive index changes.[40] It is worthwhile to note that this observation has not been fully addressed in many previous studies in which the sensitivities were compared at much different plasmon wavelengths, and the enhanced sensitivities were consequently attributed to optimization of the nanoparticle shape and size.[37,46,47] Thus, it is critical to tune the plasmon

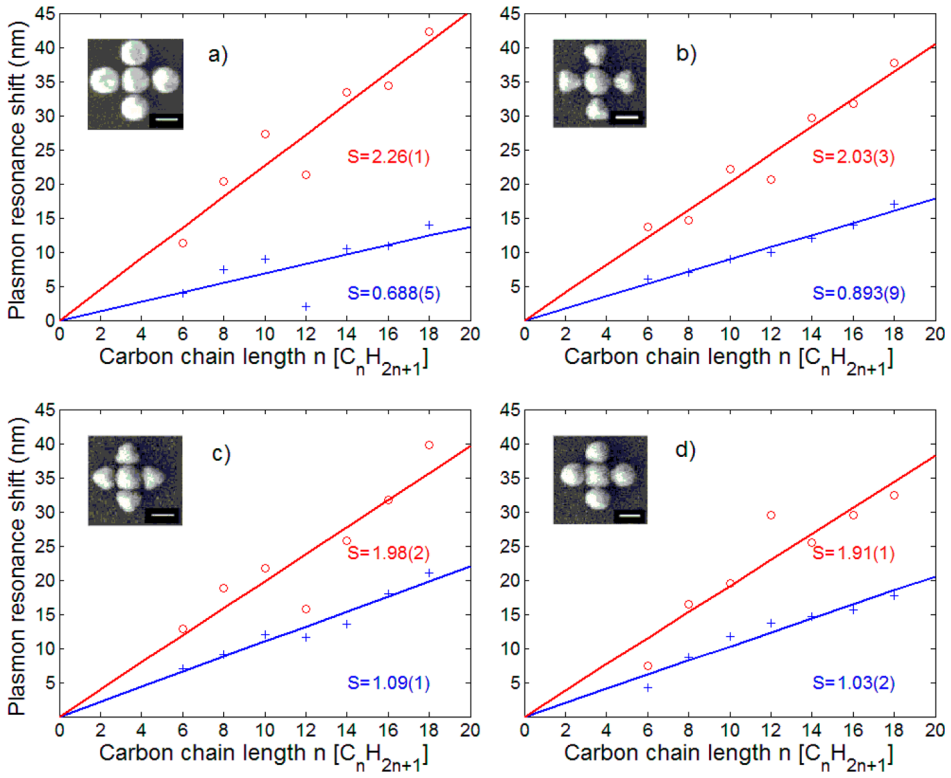

Figure 4. Monolayer sensing sensitivity of Au pentamers. (a)−(d) Extinction peak shift as a function of the carbon chain length extracted from Figure 3 for the four types of Au pentamers consisting of peripheral and central nanoparticles of different shapes as shown in the respective insets. All the symbols represent the measured points and solid lines are linear fits to the data, with red symbols/lines extracted from long-wavelength peaks and blue symbols/lines from the short-wavelength peaks. The monolayer sensitivity (S) for each nanocluster is calculated as the slope of each solid line.

resonances of different metal nanostructures at the same wavelength range in order to have a fair comparison between their refractive index sensing performance.

From Figure 4 one can also see that the monolayer sensitivity for both the long-wavelength and short-wavelength peaks is strongly affected by the constituent nanoparticle shape and arrangement in the nanoclusters. For instance, the sensing slope for the long-wavelength peak significantly decreases from 2.26 ± 0.01 nm/C-chain for the Au pentamer comprised of five identical nanodisks to 1.91 ± 0.01 nm/C-chain for a similar pentamer but with the central particle replaced by a square shape one (see Figures 4a and 4d) - even though the plasmon resonance wavelength of the former nanocluster is slightly smaller than that of the latter (see Figures 3a and 3d). In contrast, the short-wavelength peak shows a reverse behavior, with the sensing slope of the former Au pentamer being smaller than that of the latter although their peak positions are very close to each other. Such complicated behavior is clearly unexpected and beyond the previous observations that the bulk refractive index sensitivity for isolated, or more specifically, uncoupled nanoparticles increases with the plasmon wavelength.[37,44,47] This also implies that there must be other uncovered factors determining the monolayer sensing response of metal nanoclusters with strong coupling effects as we will discuss later.

Similar sensing measurements were carried out for the Au quadrumers, with results shown in Figure 5. One can see from Figures 5a−5c that the two extinction peaks of the three types of Au quadrumers comprised of different constituent nanoparticles exhibit continuous red-shifting with increasing chain length of the alkanethoil molecules. The monolayer sensitivities for the Au quadrumers were extracted following the method described above. Similar trends in the sensitivities can be clearly observed in Figures 5d−5f. For example, the long-wavelength extinction peak in the first type quadrumer (Figures 5a and 5d) exhibits the largest sensitivity although its plasmon wavelength is even smaller than that of the other two quadrumers. This further reveals that the plasmon wavelength in coupled nanoclusters is not the detrimental factor affecting the monolayer sensing sensitivity if the resonance wavelength varies in a small range. In addition, one can also see from Figures 5d−5f that spatial arrangement of individual nanoparticles in a nanocluster plays a critical role in determining the sensitivity. For example, the sensing slope for the long-wavelength peak significantly increases from 1.39 ± 0.01 nm/C-chain for the Au quadrumer comprised of three square particles and a central nanodisk to 1.93 ± 0.02 nm/C-chain for a similar quadrumer with exchanged shapes of the outside and central particles (see Figures 5e and 5f).

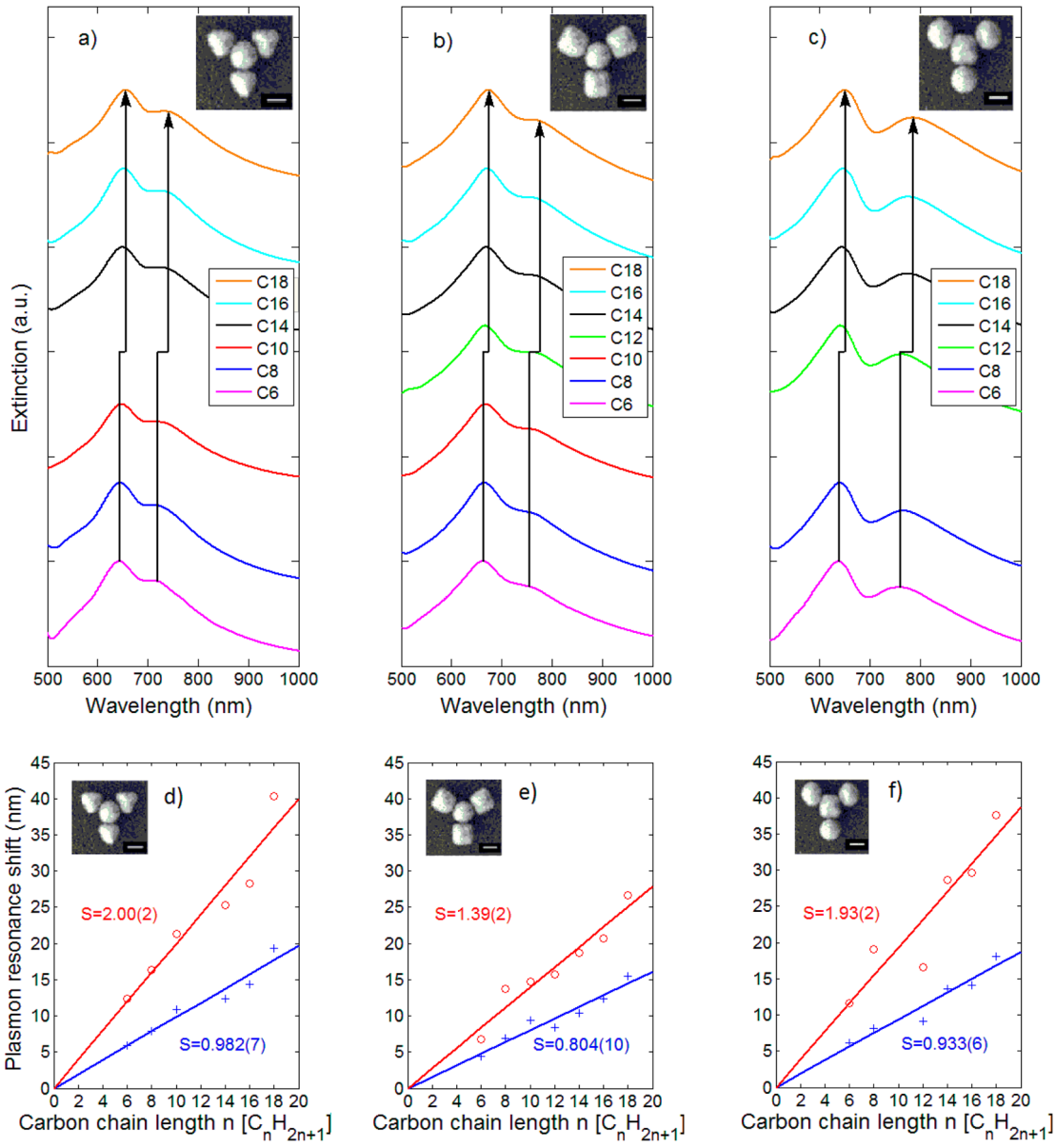

Figure 5. Plasmon resonance sensing properties of gold quadrumers. (a−c) Extinction spectra of Au pentamers adsorbed with self-assembled alkanethoils layers of different carbon chain lengths and (d−f) their corresponding sensing sensitivities. The insets show SEM images of the Au pentamers. The scale bar in each image is 100 nm. The black arrows in (a−c) are guide-to-the-eyes, indicating the total resonance shift between the top and bottom spectra.

Considering the maximum amount of plasmon resonance shift (14−42 nm) and the largest alkanethiol SAM thickness (2.0 nm) observed for plasmonic pentamers and quadrumers, we calculate the surface sensitivity of these coupled nanostructures to be 7−21 nm per monolayer of 1 nm thickness. Compared to the surface sensitivity recently predicted for single Au nanorods,[40] which is on the order of 7 nm per monolayer of 1 nm thickness at wavelength 700 nm, the coupled plasmonic oligomers demonstrate substantial sensitivity improvement, further corroborating the benefit of plasmonic coupling effects in metal nanoclusters.

Note that based on extended Mie theory and the discrete dipole approximation, Jain and El-Sayed have derived two analytical solutions to describe, respectively, the bulk refractive index sensitivities of an isolated dielectric core-metal nanoshell and an interacting nanoparticle pair. They found a universal scaling behavior for the bulk refractive index sensitivity that increases near-exponentially with a decreasing ratio of the shell thickness-to-core radius in the core−shell nanoparticle or the interparticle gap distance in the nanoparticle pair.[45,46] Unfortunately, the analytical solutions developed by Jain and El-Sayed cannot be applied to complex metal nanoclusters, simply because there are no analytical approaches to calculate the polarizabilities of such complex nanostructures. On the one hand, previous theoretical and experimental studies have also demonstrated that the bulk refractive index sensitivities for Au nanostructures of various

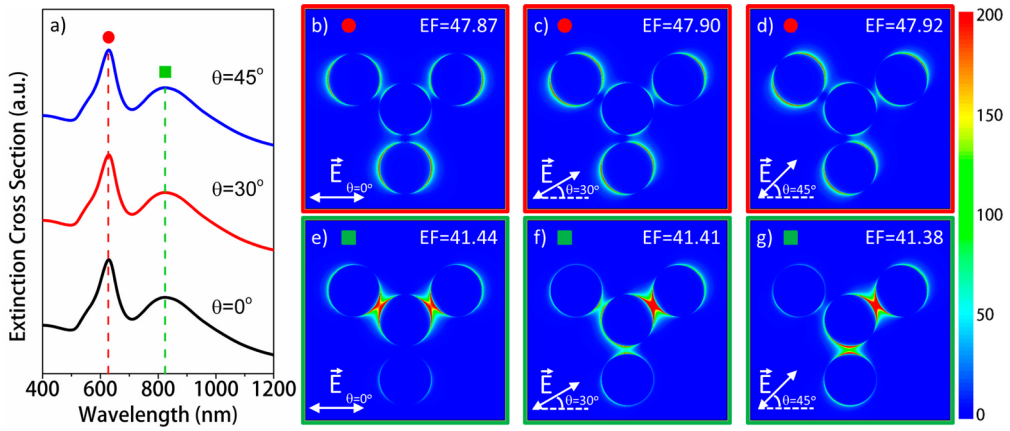

Figure 6. Incident polarization-dependent electric near-field profiles. (a) Extinction cross-section spectra of the Au quadrumer consisting of four identical circular nanodisks excited under the three indicated representative polarizations. (b−d) Normalized electric near-field intensity distribution profiles at the short-wavelength extinction peak. (e−g) The same plots for the long-wavelength extinction peak. The numbers of EF are calculated as the 3D spatially averaged intensity.

shapes have no direct correlation with their polarizabilities if the plasmon sensing wavelength is tuned to the same position by changing the nanoparticle size and shape.[35] This observation points out a potential pitfall, not addressed in the analytical solutions derived by Jain and El-Sayed, that in addition to the increase of the bulk refractive index, decreasing the nanoshell thickness or the interparticle distance also results in a large red-shift in the plasmon resonance wavelength and hence a larger sensitivity as discussed above. On the other hand, the dipole−dipole approximation used by Jain and El-Sayed are based on simple consideration of dipolar moments of a couple of small sub-100 nm nanoparticles, which cannot be applied for relatively larger metal nanostructures of wavelength-comparable dimensions due to strong retardation effect. Moreover, existence of more than two nanoparticles makes the situation more complex than nanoparticle dimers as the plasmonic interference effect becomes pronounced in determining the absorption and scattering response.[50]

In general, it has been postulated that the refractive index sensitivity of a localized surface plasmon resonance is closely related to the near-field EF and the degree of field localization in the metal nanoparticle, which is supported by many experimental results. Metal nanostructures with sharp geometric features such as nanoprisms, nanobranches, and nanobipyramids usually exhibit higher sensitivities than more conventional nanoparticles including nanospheres, nanocubes, and nanorods.[37,38,44]

In light of this complex behavior and in order to adequately understand the observed monolayer sensing response, we have performed full-wave electromagnetic simulations to study the near-field properties of the Au nanoclusters using the finite-difference-time-domain method (FDTD), aiming at providing an intuitive physical scenario for understanding these oligomer clusters. Since the sensing experiments were carried out with unpolarized light at normal incidence, we have calculated the electric near-field distribution profiles at three representative incident polarizations by considering the symmetries in the Au pentamers and quadrumers. Figure 6 renders the two-dimensional contour plots of the field distribution for the Au quadrumer consisting of four identical nanodisks at its two extinction peaks. Interestingly, each near-field profile at the three incident polarizations for the short-wavelength peak (see Figures 6b−6d) actually exhibits more "hot" spots (around each nanodisk) but with lower intensity than the long-wavelength peak, where the enhanced field concentrates at gaps between nanodisks (see Figures 6e−6g). The same behavior was observed for the other Au quadrumers and pentamers though their constituent nanoparticle shape and the nanocluster symmetry are different from the example nanocluster.

To further unveil the actual factors affecting the monolayer sensitivity, we have integrated the electric-field intensity over the whole nanocluster surface and interparticle gaps (where the alkanethoil molecules adsorbed) to obtain a spatially averaged EF (integrated over the lateral adsorption region of alkanethiol molecules) for each nanocluster at the two extinction peaks. Such treatment should be more reliable than calculating the maximum field EF,[38] because the analytes are adsorbed over the whole nanocluster rather than simply at the specific sites where there is maximum enhancement. The results demonstrate that the averaged EF has little dependence on the incident polarization for the Au quadrumer (see the numbers for EF in Figure 6), and this observation also holds true for the other quadrumers and pentamers.

Figure 7 plots the measured sensitivities and the calculated averaged EFs at both extinction peaks for each nanocluster. In order to disclose the influence of shape change on EF, isolated nanoclusters were simulated, where separation between adjacent nanoparticles

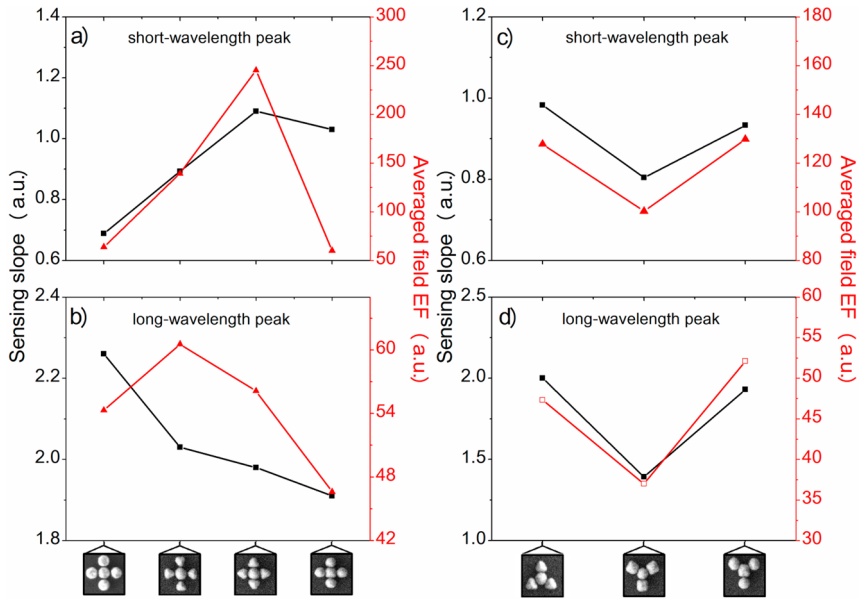

Figure 7. Comparison between spatially averaged electric-field intensity enhancement and the measured monolayer sensing slope for the Au pentamers and quadrumers. The black squares are the calculated sensing slopes extracted from Figure 5, and the red triangles are the calculated average field EFs. The solid lines are guides to the eye and aid in showing a correlative trend between the sensing slope and the averaged field EF.

is slightly altered by ±2 nm by taking into account plasma etching-induced shape change. A direct comparison between them clearly shows a correlation between the measured sensing slope and the calculated EF for all the pentamers (Figures 7a and 7b) and quadrumers (Figures 7c and 7d) though some slight discrepancies can still be seen in a few cases. This correlation provides direct evidence that the monolayer sensing response of coupled plasmonic nanoclusters is closely related to the spatially averaged near-field enhancement. Note that the discrepancy between the sensing slope and the averaged EF occurring for the pentamer consisting of a square particle surrounded by four nanodisks (see Figure 7a) and for the pentamer consisting of five identic nanodisks (see Figure 7b) might be due to the use of the same rounding radius for all nanoparticle systems. For a fair comparison of the averaged EF among all the systems, in our simulations the corners in square and triangular particles are blunted with a rounding radius of 10 nm, which may deviate from realistic situations. In particular, the near field associated with the short-wavelength peak is mainly concentrated at the corners of the square particle, resulting in a strong dependence of the averaged EF on the rounding radius (results not shown).

We also note that, in Figures 4 and 5, the plasmon resonance shift shows a linear dependence on carbon chain length for both plasmonic pentamers and quadrumers. This dependence is counterintuitive as the plasmonic near-field decays very rapidly from the surface of the particles, generally following an exponential decaying function. Here we apply the electromagnetic perturbation theory to explain this behavior. The application of the perturbation theory to our case is valid as the effect refractive index change Δn (on the order of 0.02 to 0.05, roughly estimated from the bulk refractive index sensitivity of plasmonic oligomers S and our experimentally observed plasmon resonance shift $\Delta\lambda$ using the equation $\Delta n = \Delta\lambda/S$) induced by the adsorption of molecular monolayers is significantly smaller than that of the surrounding environment n. The theory predicts that the original resonant wavelength λ of an optical resonator shifts by an amount of $\Delta\lambda$ given by $\Delta\lambda = \lambda/n \cdot \Delta n \cdot V_E$, where V_E is the fraction of electric-field energy inside the perturbation region,[34,51] *i.e.* a nanoshell of various thickness concentric with the nanoparticles. In ref 51, Joannopoulos *et al.* pointed out that the electric field tends to concentrate in high-index medium to minimize the Rayleigh quotient of an optical system. This leads to tighter field localization in the molecular monolayer region and produces a larger value for V_E, which gives rise to the red-shift in the extinction peaks of the plasmonic nanoclusters.

Following the equation described above, on the one hand, we calculated V_E as a function of the dimension of the perturbation region at the two extinction peaks for the plasmonic pentamer consisting of five identical nanodisks. Figure 8 shows that V_E follows a linear relationship with the perturbation dimension, *i.e.* the thickness of the nanoshell used. Calculations performed for other plasmonic nanoclusters also exhibit a linear dependence. On the other hand, previous ellipsometric measurements demonstrated that the thickness of a molecular monolayer self-assembled on polycrystalline gold film linearly increases with carbon chain length when a constant effective refractive index

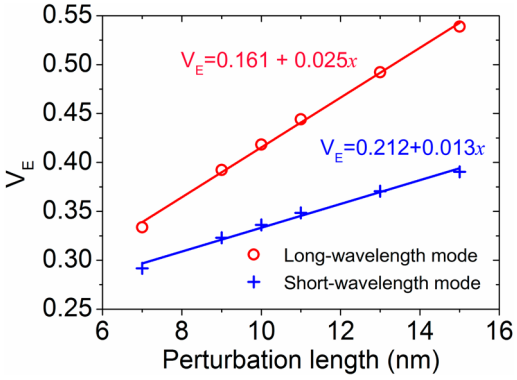

Figure 8. Fraction of electric-field energy inside the perturbation region as a function of the perturbation length for the Au pentamer consisting of five identical nanodisks. The symbols are from calculations and the solid lines are linear fits to the calculation results, with the fitting equations shown as insets.

was used in ellipsometric modeling.[44,49] This points out that the refractive index change Δn should also be linearly dependent on the length of the molecular monolayer. As a result, we can conclude from the equation described above that the plasmon resonance shift also shows a linear dependence on the carbon chain length instead of exponential or other complex dependences. Note that the perturbation lengths used in our calculations are much larger the thicknesses of the alkanethiol monolayers, because the computation power cannot afford to mesh the three-dimensional nanoparticles with mesh size down to less than 0.1 nm if the actual monolayer thicknesses were considered as the perturbation lengths.

CONCLUSIONS

In conclusion, we have experimentally studied the monolayer sensing response of plasmonic Au nanoclusters and found that the sensitivity of each nanocluster has a strong dependence on the constituting nanoparticle shape and spatial arrangement. Direct comparison between the measured monolayer detection sensitivity and the calculated near-field profile at respective plasmon resonance wavelengths reveals that the sensitivity is largely related to the spatially averaged near-field EF. Our results offer many implications for optimizing the monolayer sensing performance of plasmonic nanoclusters-based biosensors and may also open up the possibilities for using plasmonic nanoclusters for single-molecule detection and identification.

METHODS

Fabrication and Characterization of Au Quadrumers and Pentamers. Arrays of Au quadrumers and pentamers consisting of differently shaped components were fabricated on the same quartz substrate by EBL (Elonix 100 kV EBL system). Each array has a dimension of 50 $\times$ 50 μm^2 and consists of 60 nm thick Au nanoparticles of different shapes, all with 140 nm nominal lateral dimension. A three nanometer thick Ti film was deposited on the substrate by e-beam evaporation (EB03 BOC Edwards) to increase the adhesion between Au and quartz, followed by the evaporation of a 60 nm Au film and spin-coating of 50 nm of hydrogen silsesquioxane (HSQ) as a negative electroresist. After baking the sample at 200 °C for 2 min, a combined process of e-beam exposure, chemical development, and ion-milling was performed to create well-defined Au oligomers on the substrate. The surface morphology of fabricated structures was characterized by high-resolution scanning electron microscopy (SEM) and atomic force microscopy (AFM). Fourier transform infrared spectroscopy (FTIR, Bruker Hyperion 2000 with a Vertex 70) was used to measure the extinction, defined as (1 - Transmission), through each array at normal incidence with an unpolarized white light, before and after adsorption of each self-assembled alkanethiol monolayer.

Preparation, Adsorption, and Removal of Alkanethiol Monolayers. Before adsorption of the self-assembled monolayer (SAM), the nanocluster sample was rinsed with 2-propanol and etched with an oxygen plasma at 60 W for 3 min in order to remove any contaminants. Linear alkanethiols with different chain lengths were used, including 1-hexanethiol, 1-octanethiol, 1-decanethiol, 1-dodecanethiol, 1-tetradecanethiol, 1-hexadecanethiolm and 1-octadecanethiol. All alkanethiols were purchased from Sigma-Aldrich. The nanocluster sample was incubated in a 5 mM solution of each alkanethiol in ethanol for 24 h. The sample was then rinsed with ethanol, and its extinction response was characterized by FTIR. To remove the SAM, the sample was etched twice with oxygen plasma at 60 W for 5 min and rinsed with ethanol after each etching.

Full-Wave Numerical Calculations of the near-Field Intensity Enhancement. Three-dimensional (3D) full-wave electromagnetic simulations were performed to calculate the electric near-field distribution and field intensity enhancement of each nanocluster using a commercially available finite-difference-time domain code (Lumerical FDTD). The dielectric constants of Au used in the simulations were extracted from Johnson and Christy data.[52] The EFs were calculated for isolated nanoclusters encompassed by perfected matched layer (PML) boundaries in all directions. Different from some previous studies, a full consideration of the substrate effect was made in our simulations. To account for the blunting effect of particles caused by imperfect fabrication as well as plasma etching, all the corners in triangular and rectangle particles were rounded with a radius of 10 nm. The diameter of circular disk and the lateral length of other shapes of nanoparticles were set to be 130 $\pm$ 2 nm and 120 $\pm$ 4 nm, respectively, which results in a gap separation between adjacent particles in each nanocluster to be 30 $\pm$ 2 nm in order to have the best match between experimental and simulation results. The height of all particles was set to be 60 nm. In the calculations, the incident electric field is polarized along the horizontal axis, and the mesh size used around the edges of the nanoparticles is as small as 0.5 nm. The spatially averaged electric field intensity enhancement factor (EF) was calculated as $|\|^2/|E_0|^2$, where $|\|^2$ is the local field intensity and $|E_0|^2$ is the incident field intensity. A frequency-domain 3D monitor for recording the near-field profiles of 11 XY planes was defined from the substrate surface to the top surface of the clusters, generating a total number of 10^5 data points for precisely calculating the averaged near-field intensity. Since the wavelength shift is caused by the coverage of molecular monolayers, the total field within the adsorption region is summed up for SAMs of different carbon chain lengths.

Conflict of Interest: The authors declare no competing financial interest.

Acknowledgment. The authors acknowledge the financial support from the United Kingdom Engineering and Physical Sciences Research Council (EPSRC), the Hong Kong Research Grants Council (ECS Grant No. 509513), the Natural Science Foundation of China (Grant No. 11304261), and the Leverhulme

Trust Foundation. M.K. acknowledges the support by the European Science Foundation ESF Short Visit Grants (Grant No. 5137). M.R. and M.H. acknowledge the use of the facilities of Data Storage Institute, (A*STAR) Agency for Science, Technology and Research, Singapore for sample fabrication and SEM Imaging. L.Z. and C.-W.Q. acknowledge the financial support from the National University of Singapore (Grant No. R-263-000-A45-112).

REFERENCES AND NOTES

1. Anker, J. N.; Hall, W. P.; Lyandres, O.; Shah, N. C.; Zhao, J.; van Duyne, R. P. Biosensing with Plasmonic Nanosensors. *Nat. Mater.* **2008**, *7*, 442–453.
2. Lal, S.; Link, S.; Halas, N. J. Nano-Optics from Sensing to Waveguiding. *Nat. Photonics* **2007**, *1*, 641–648.
3. Stewart, M. E.; Anderton, C. R.; Thompson, L. B.; Marin, J.; Gray, S. K.; Rogers, J. A.; Nuzzo, R. G. Nanostructured Plasmonic Sensors. *Chem. Rev.* **2008**, *108*, 494–521.
4. Larsson, E. M.; Langhammer, C.; Zoric, I.; Kasemo, B. Nanoplasmonic Probes of Catalytic Reactions. *Science* **2009**, *326*, 1091–1094.
5. Shan, X. N.; Patel, U.; Wang, S. P.; Iglesias, R.; Tao, N. J. Imaging Local Electrochemical Current *via* Surface Plasmon Resonance. *Science* **2010**, *327*, 1363–1366.
6. Lei, D. Y.; Appavoo, K.; Sonnefraud, Y.; Haglund, R. F.; Maier, S. A. Single-Particle Plasmon Resonance Spectroscopy of Phase Transition in Vanadium Dioxide. *Opt. Lett.* **2010**, *35*, 3988–3990.
7. Appavoo, K.; Lei, D. Y.; Sonnefraud, Y.; Wang, B.; Pantelides, S. T.; Maier, S. A.; Haglund, R. F. Role of Defects in the Phase Transition of VO_2 Nanoparticles Probed by Plasmon Resonance Spectroscopy. *Nano Lett.* **2012**, *12*, 780–786.
8. Liedberg, B.; Nylander, C.; Lundstrom, I. Surface-Plasmon Resonance for Gas-Detection and Biosensing. *Sens. Actuators* **1983**, *4*, 299–304.
9. Liu, N.; Tang, M. L.; Hentschel, M.; Giessen, H.; Alivisatos, A. P. Nanoantenna-Enhanced Gas Sensing in a Single Tailored Nanofocus. *Nat. Mater.* **2011**, *10*, 631–636.
10. Shen, Y.; Zhou, J.; Liu, T.; Tao, Y.; Jiang, R.; Liu, M.; Xiao, G.; Zhu, J.; Zhou, Z.-K.; Wang, X.; *et al.* Plasmonic Gold Mushroom Arrays with Refractive Index Sensing Figures of Merit Approaching the Theoretical Limit. *Nat. Commun.* **2013**, *4*, 2381.
11. Sherry, L. J.; Chang, S.-H.; Schatz, G. C.; Van Duyne, R. P. Localized Surface Plasmon Resonance Spectroscopy of Single Silver Nanocubes. *Nano Lett.* **2007**, *5*, 2034–2038.
12. Markus, M. A.; Lei, D. Y.; Wondraczek, L.; Naval, V.; Maier, S. A. Hybrid Nanoparticle-Microcavity Based Plasmonic Nanoprobes with Simultaneous Local and Remote Sensing Abilities. *Nat. Commun.* **2012**, *3*, 1108.
13. Mayer, K. M.; Hafner, J. H. Localized Surface Plasmon Resonance Sensors. *Chem. Rev.* **2011**, *111*, 3828–3857.
14. Chen, H. J.; Shao, L.; Li, Q.; Wang, J. F. Gold Nanorods and Their Plasmonic Properties. *Chem. Soc. Rev.* **2013**, *42*, 2679–2724.
15. Halas, N. J.; Lal, S.; Chang, W.-S.; Link, S.; Nordlander, P. Plasmons in Strongly Coupled Metallic Nanostructures. *Chem. Rev.* **2011**, *111*, 3913–3961.
16. Miroshnichenko, A. E.; Flach, S.; Kivshar, Y. S. Fano Resonances in Nanoscale Structures. *Rev. Mod. Phys.* **2010**, *82*, 2257–2298.
17. Prodan, E.; Radloff, C.; Halas, N. J.; Nordlander, P. A Hybridization Model for the Plasmon Response of Complex Nanostructures. *Science* **2003**, *302*, 419–422.
18. Aubry, A.; Lei, D. Y.; Maier, S. A.; Pendry, J. B. Interaction between Plasmonic Nanoparticles Revisited with Transformation Optics. *Phys. Rev. Lett.* **2010**, *105*, 233901.
19. Rahmani, M.; Lei, D. Y.; Giannini, V.; Lukiyanchuk, B.; Ranjbar, M.; Liew, T. Y. F.; Hong, M.; Maier, S. A. Subgroup Decomposition of Plasmonic Resonances in Hybrid Oligomers: Modeling the Resonance Lineshape. *Nano Lett.* **2012**, *12*, 2101–2106.
20. Zhang, S.; Genov, D. A.; Wang, Y.; Liu, M.; Zhang, X. Plasmon-Induced Transparency in Metamaterials. *Phys. Rev. Lett.* **2008**, *101*, 047401.
21. Liu, N.; Langguth, L.; Weiss, T.; Kästel, J.; Fleischhauer, M.; Pfau, T.; Giessen, H. Plasmonic Analogue of Electromagnetically Induced Transparency at the Drude Damping Limit. *Nat. Mater.* **2009**, *8*, 758–762.
22. Hao, F.; Sonnefraud, Y.; Dorpe, P. V.; Maier, S. A.; Halas, N. J.; Nordlander, P. Symmetry Breaking in Plasmonic Nanocavities: Subradiant LSPR Sensing and a Tunable Fano Resonance. *Nano Lett.* **2008**, *8*, 3983–3988.
23. Verellen, N.; Sonnefraud, Y.; Sobhani, H.; Hao, F.; Moshchalkov, V. V.; Dorpe, P. V.; Nordlander, P.; Maier, S. A. Fano Resonances in Individual Coherent Plasmonic Nanocavities. *Nano Lett.* **2009**, *9*, 1663–1666.
24. Fan, J. A.; Wu, C.; Bao, K.; Bao, J.; Bardhan, R.; Halas, N. J.; Manoharan, V. N.; Nordlander, P.; Shvets, G.; Capasso, F. Self-Assembled Plasmonic Nanoparticle Clusters. *Science* **2010**, *328*, 1135.
25. Sheikholeslami, S.; Jun, Y.-W.; Jain, P. K.; Alivisatos, A. P. Coupling of Optical Resonances in a Compositionally Asymmetric Plasmonic Nanoparticle Dimer. *Nano Lett.* **2010**, *10*, 2655–2660.
26. Lassiter, J. B.; Sobhani, H.; Fan, J. A.; Kundu, J.; Capasso, F.; Nordlander, P.; Halas, N. J. Fano Resonances in Plasmonic Nanoclusters: Geometrical and Chemical Tunability. *Nano Lett.* **2010**, *10*, 3184–3189.
27. Fan, J. A.; Bao, K.; Wu, C.; Bao, J.; Bardhan, R.; Halas, N. J.; Manoharan, V. N.; Shvets, G.; Nordlander, P.; Capasso, F. Fano-like Interference in Self-Assembled Plasmonic Quadrumer Clusters. *Nano Lett.* **2010**, *10*, 4680–4685.
28. Sonnefraud, Y.; Verellen, N.; Sobhani, H.; Vandenbosch, G. A. E.; Moshchalkov, V. V.; Dorpe, P. V.; Nordlander, P.; Maier, S. A. Experimental Realization of Subradiant, Superradiant, and Fano Resonances in Ring/Disk Plasmonic Nanocavities. *ACS Nano* **2010**, *4*, 1664–1670.
29. Verellen, N.; Dorpe, P. V.; Huang, C.; Lodewijks, K.; Vandenbosch, G. A. E.; lagae, L.; Moschalkov, V. V. Plasmon Line Shaping Using Nanocrosses for High Sensitivity Localized Surface Plasmon Resonance Sensing. *Nano Lett.* **2011**, *11*, 391–397.
30. Lovera, A.; Gallinet, B.; Nordlander, P.; Martin, O. J. F. Mechanisms of Fano Resonances in Coupled Plasmonic Systems. *ACS Nano* **2013**, *7*, 4527–4536.
31. Miroshnichenko, A. E.; Kivshar, Y. S. Fano Resonances in All-Dielectric Oligomers. *Nano Lett.* **2012**, *12*, 6459–6463.
32. Shafiei, F.; Monticone, F.; Le, K. Q.; Liu, X. X.; Hartsfield, T.; Alù, A.; Li, X. A Subwavelength Plasmonic Metamolecules Exhibiting Magnetic-Based Optical Fano Resonance. *Nat. Nanotechnol.* **2013**, *8*, 95–99.
33. Rahmani, M.; Lukiyanchuk, B.; Hong, M. Fano Resonance in Novel Plasmonic Nanostructures. *Laser Photonics Rev.* **2013**, *7*, 329–349.
34. Gallinet, B.; Martin, O. J. F. Refractive Index Sensing with Subradiant Modes: A Framework To Reduce Losses in Plasmonic Nanostructures. *ACS Nano* **2013**, *7*, 6978–6987.
35. Zhan, Y.; Lei, D. Y.; Li, X.; Maier, S. A. Plasmonic Fano Resonances in Nanohole Quadrumers for Ultra-sensitive Refractive Index Sensing. *Nanoscale* **2014**, *6*, 4705–4715.
36. Yong, Z.; Lei, D. Y.; Lam, C. H.; Wang, Y. Ultrahigh Refractive Index Sensing Performance of Plasmonic Quadrupole Resonances in Gold Nanoparticles. *Nanoscale Res. Lett.* **2014**, *9*, 187.
37. Chen, H. J.; Kou, X. S.; Yang, Z.; Ni, W. H.; Wang, J. F. Shape- and Size-Dependent Refractive Index Sensitivity of Gold Nanoparticles. *Langmuir* **2008**, *24*, 5233–5237.
38. Chen, H. J.; Shao, L.; Woo, K. C.; Ming, T.; Lin, H. Q.; Wang, J. F. Shape-Dependent Refractive Index Sensitivities of Gold Nanocrystals with the Same Plasmon Resonance Wavelength. *Langmuir* **2008**, *24*, 5233–5237.
39. Anker, J. N.; Hall, W. P.; Lyandres, O.; Shah, N. C.; Zhao, J.; Van Duyne, R. P. Biosensing with Plasmonic Nanosensors. *Nat. Mater.* **2008**, *7*, 442–453.
40. Otte, M. A.; Sepúlveda, B.; Ni, W. H.; Juste, J. P.; Liz-Marzán, L. M.; Lechuga, L. M. Identification of the Optimal Spectral Region for Plasmonic and Nanoplasmonic Sensing. *ACS Nano* **2010**, *4*, 349–357.

41. Yu, X.; Lei, D. Y.; Amin, F.; Hartmann, R.; Acuna, G. P.; Guerrero-Martínez, A.; Maier, S. A.; Tinnefeld, P.; Carregal-Romero, S.; Parak, W. J. Distance-Control in-between Plasmonic Nanoparticles *via* Biological and Polymeric Spacers. *Nano Today* **2013**, *8*, 480–493.
42. Barrow, S. J.; Funston, A. M.; Wei, X.; Mulvaney, P. DNA-Directed Self-Assembly and Optical Properties of Discrete 1D, 2D and 3D Plasmonic Structures. *Nano Today* **2013**, *8*, 138–167.
43. Liu, G. L.; Yin, Y.; Kunchakarra, S.; Mukherjee, B.; Gerion, D.; Jett, S. D.; Bear, D. G.; Gray, J. W.; Alivisatos, A. P.; Lee, L. P.; *et al.* A Nanoplasmonic Molecular Ruler for Measuring Nuclease Activity and DNA Footprinting. *Nat. Nanotechnol.* **2006**, *1*, 47–52.
44. Hill, R. T.; Hucknall, A.; Wolter, S. D.; Jokerst, N. M.; Smith, D. R.; Chilkoti, A. Plasmonic Ruler with Angstrom Length Resolution. *ACS Nano* **2013**, *6*, 9237–9246.
45. Larsson, E. M.; Alegret, J.; Käll, M.; Sutherland, D. S. Sensing Characteristics of NIR Localized Surface Plasmon Resonances in Gold Nanorings for Application as Ultrasensitive Biosensors. *Nano Lett.* **2007**, *7*, 1256–1263.
46. Jain, P. K.; El-Sayed, M. A. Surface Plasmon Resonance Sensitivity of Metal Nanostructures: Physical Basis and Universal Scaling in Metal Nanoshells. *J. Phys. Chem. C* **2007**, *111*, 17451–17454.
47. Jain, P. K.; El-Sayed, M. A. Noble Metal Nanoparticles Pairs: Effect of Medium for Enhanced Nanosensing. *Nano Lett.* **2008**, *8*, 4347–4352.
48. Lei, D. Y.; Wan, J. T. K.; Ong, H. C. Numerical and Analytical Evaluations of the Sensing Sensitivity of Waveguide Mode in One-Dimensional Metallic Gratings. *Nanotechnology* **2012**, *23*, 275501.
49. Biebuyck, H. A.; Bain, C. D.; Whitesides, G. M. Comparison of Organic Monolayers on Polycrystalline Gold Spontaneously Assembled from Solutions Containing Dialkyl Disulfides or Alkanethoils. *Langmuir* **1994**, *10*, 1825–1831.
50. Rahmani, M.; Miroshnichenko, A. E.; Lei, D. Y.; Luk'yanchuk, B.; Tribelsky, M. I.; Kuznetsov, A. I.; Kivshar, Y. S.; Francescato, Y.; Giannini, V.; Hong, M.; Maier, S. A. Beyond the Hybridization Effects in Plasmonic Nanoclusters: Diffraction-Induced Enhanced Absorption and Scattering. *Small* **2014**, *10*, 576–583.
51. Joannopoulos, J. D.; Johnson, S. G.; Winn, J. N.; Meade, R. D. *Photonic Crystals: Modeling the Flow of Light*, 2nd ed.; Princeton University Press: Princeton, NJ, 2008.
52. Johnson, P. B.; Christy, R. W. Optical Constants of the Noble Metals. *Phys. Rev. B* **1972**, *6*, 4370–4379.